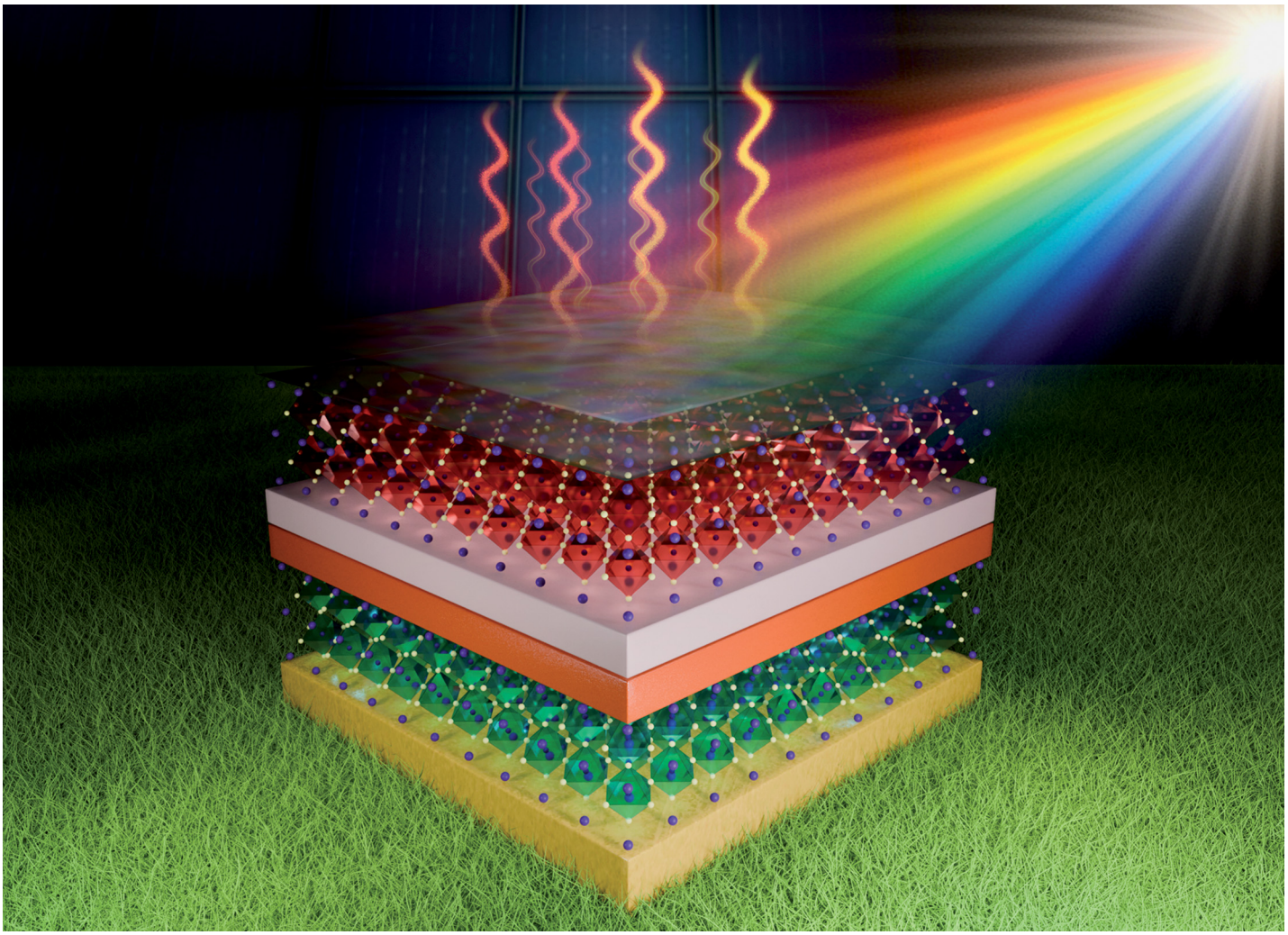

Showcasing collaborative research led by Prof. George Kakavelakis of Hellenic Mediterranean University and Dr George Perrakis of Foundation for Research and Technology – Hellas

Solar photons beyond the band gap wavelengths: their effect on solution-processed solar cells

This international research collaboration explores the contribution of infrared light beyond band gap wavelengths on the temperature and performance of single-junction and tandem solution-processed solar cells. It examines the physical origin and interplay of parasitic absorption and conversion losses as a function of band gap, aiming to enhance device stability and power conversion efficiency. Results show up to seven times lower efficiency losses compared to silicon solar cells, highlighting their sustainability potential.

Image reproduced by permission of the authors from *Mater. Horiz.*, 2025, **12**, 2922.

As featured in:

See George Perrakis, George Kakavelakis *et al.*, *Mater. Horiz.*, 2025, **12**, 2922.

ROYAL SOCIETY OF CHEMISTRY

rsc.li/materials-horizons

Registered charity number: 207890

Materials Horizons

ROYAL SOCIETY OF CHEMISTRY

COMMUNICATION

View Article Online
View Journal | View Issue

Cite this: *Mater. Horiz.*, 2025, **12**, 2922

Received 29th January 2025,
Accepted 24th March 2025

DOI: 10.1039/d5mh00186b

rsc.li/materials-horizons

Solar photons beyond the band gap wavelengths: their effect on solution-processed solar cells†

George Perrakis,*[a] Apostolos Panagiotopoulos,[b] Temur Maksudov,[c] Chrysa Aivalioti,[c] Essa A. Alharbi,[cd] Shadi Fatayer,[c] Martin Heeney,[c] Anna C. Tasolamprou,[e] George Kenanakis,[a] Konstantinos Petridis,[f] Thomas D. Anthopoulos,[cg] S. Ravi P. Silva,[b] Michael Graetzel,[h] Maria Kafesaki[ai] and George Kakavelakis*[f]

A deep understanding of how solution-processed solar cells (SSCs) perform under varying temperatures and irradiance is crucial for their optimal design, synthesis, and use. However, current partial spectral characterization, primarily below the band gap wavelengths ($\lambda < \lambda_g$), limits insights into their full operation. In this work, we expand the current knowledge by providing comprehensive full-spectrum experimental optical characterizations (~300–2500 nm) and theoretical optical-thermal-electrical analysis for the most common high-efficiency single-junction and tandem organic SSCs (OSCs) and perovskite SSCs (PSCs), including p–i–n OSC, n–i–p OSC, p–i–n PSC, n–i–p mesoscopic PSC, OSC/PSC, and PSC/PSC. By incorporating solar photons above λ_g in our investigation, we uncover the effects of parasitic absorption (~300–2500 nm) and conversion losses ($\lambda < \lambda_g$) on operating temperature and power conversion efficiency (PCE) losses, highlighting the conditions, materials, and optimal architectures for reducing device temperature. These improvements could reduce PCE losses by up to ~7 times compared to conventional silicon wafer-based solar cells in real-world conditions.

New concepts

In this work we access the influence of IR light beyond the band gap wavelength (λ_g) on solution processed solar cells (SSCs) operation, in order to uncover the physical origin and interplay of parasitic absorption (~300–2500 nm) and conversion losses (~300–λ_g nm) that leads to more stable SSCs with higher power conversion efficiencies (PCEs). Through a detailed optical-thermal-electrical analysis, we provide guidelines towards the design of more efficient SSC architectures. A key finding is the identification of optimal device structures and materials that reduce operating temperatures and minimize PCE losses—up to seven times lower than in conventional silicon solar cells. We also uncover the overlooked contribution of TCEs, such as ITO and FTO, as parasitic heat sources and propose alternatives like graphene and carbon nanotubes for improved thermal management. Additionally, we highlight charge transport layers (*e.g.*, PEDOT:PSS, Spiro-OMeTAD) and electrodes (Cu) and expanded band tail states in perovskites as significant contributors to parasitic absorption. Importantly, our analysis challenges the assumption that tandem SSCs fundamentally outperform single-junction counterparts, showing that spectral utilization inefficiencies introduce substantial PCE losses. We propose voltage optimization as a key design strategy. By integrating materials science, photonics, and solar energy engineering, our work provides actionable strategies for reducing thermal losses, optimizing device architecture, and advancing the commercialization of SSCs with enhanced stability and efficiency.

Introduction

Current studies on solution-processed solar cells (SSCs), *e.g.*, thin-film organic solar cells (OSCs),[1,2] perovskite solar cells (PSCs),[3–5] and their tandems (OSC/PSC and PSC/PSC),[6–8] focus solely on the absorption properties of the device at wavelengths

[a] *Institute of Electronic Structure and Laser (IESL), Foundation for Research and Technology – Hellas (FORTH), 70013 Heraklion, Crete, Greece. E-mail: gperrakis@iesl.forth.gr*
[b] *Advanced Technology Institute (ATI), Department of Electrical and Electronic Engineering, University of Surrey, Guildford, Surrey GU2 7XH, UK*
[c] *KAUST Solar Center (KSC), Physical Sciences and Engineering Division (PSE), King Abdullah University of Science and Technology (KAUST), Thuwal 23955-6900, Saudi Arabia*
[d] *Microelectronics and Semiconductor Institute, King Abdulaziz City for Science and Technology (KACST), Riyadh 11442, Saudi Arabia*
[e] *Department of Physics, National and Kapodistrian University of Athens, 15784 Athens, Greece*
[f] *Department of Electronic Engineering, School of Engineering, Hellenic Mediterranean University, Romanou 3, Chalepa, Chania, Crete GR-73100, Greece. E-mail: kakavelakis@hmu.gr*
[g] *Henry Royce Institute and Photon Science Institute, Department of Electrical and Electronic Engineering, The University of Manchester, Oxford Road, Manchester M13 9PL, UK*
[h] *Laboratory of Photonics and Interfaces, Institute of Chemical Sciences and Engineering, Ecole Polytechnique Federal de Lausanne, Lausanne 1015, Switzerland*
[i] *Department of Materials Science and Engineering, University of Crete, 70013 Heraklion, Crete, Greece*

† Electronic supplementary information (ESI) available. See DOI: https://doi.org/10.1039/d5mh00186b

below the band gap wavelength of the lowermost sub-cell energy gap ($\lambda < \lambda_g$) ($\lambda_g \sim$ 800 and ~1000 nm for PSCs and OSCs/tandems, respectively),[1–11] whereas the sun has considerable intensity also in infrared (IR) wavelengths up to ~2500 nm. This partial spectral characterization (at $\lambda < \lambda_g$) limits our understanding on their operation, *i.e.*, operating temperature, power conversion efficiency (PCE), and output-power losses relative to standard testing conditions (STC – 1000 W m^{-2} of solar radiation and 25 °C).

Specifically, a significant part of the solar electromagnetic radiation absorbed by the solar cell ($\lambda < \lambda_g$) is converted into heat due to practical and thermodynamic limitations to solar energy conversion, *e.g.*, carriers' non-radiative recombination and thermalization.[12–15] Heating further increases due to parasitic absorption of incident photons (~300–2500 nm) at the various functional materials, *e.g.*, hole-transport layers (HTLs), electron-transport layers (ETLs), transparent conductive oxide (TCO) or metal contacts.[1–11,16,17] Consequently, operating temperature increases due to solar heating arising from (i) conversion losses (for $\lambda < \lambda_g$) and (ii) parasitic absorption (~300–2500 nm). Moreover, PCE decreases, due to solar cells' negative voltage-temperature coefficient,[18] increasing output-power losses relative to STC.

Due to the partial spectral characterization (*i.e.*, at $\lambda < \lambda_g$) in all the literature to date,[1–11,16,17,19] the amount of heating in SSCs has not been identified and clearly understood. Therefore, the relative impact (as well as the interplay) of heat generated due to parasitic absorption (~300–2500 nm) *versus* conversion losses (for $\lambda < \lambda_g$) remains unclear. This constitutes an intricate problem given (i) the wide range of the organic and perovskite semiconductors with continuously tunable band gaps, different chemical composition, and properties,[6–8] (ii) technology versatility, *i.e.*, various architectures, such as planar or mesoporous n–i–p,[2–4] p–i–n,[1,5] or their tandems,[6–8] with various functional materials, such as various HTLs, ETLs, TCOs, or metal contacts,[1–11,17,20,21] (iii) varying environmental conditions,[22,23] as well as (iv) the inherent complexity of the required optical, electrical, and thermal analysis.[12–14] As a result, partial spectral characterization (at $\lambda < \lambda_g$) limits our understanding on SSCs' optimal architecture, λ_g, or material requirements.

Herein, we expand the current knowledge for more stable SSCs with higher PCEs by providing full spectrum analysis beyond λ_g (~300–2500 nm) for a wide range of high-efficiency single-junction and tandem organic and perovskite SSCs, namely (i) p–i–n OSC,[1] (ii) n–i–p OSC,[2] (iii) p–i–n PSC,[5] (iv) n–i–p mesoscopic PSC,[4] (v) OSC/PSC,[6] and (vi) PSC/PSC.[7] Despite their thin-film nature (~1 μm),[1–11] experimental characterization shows substantial IR absorption in all such cases. Simulations indicate that IR absorption occurs mainly within the front TCO contacts, specifically within indium tin oxide (ITO) and fluorine-doped tin oxide (FTO), as well as within perovskites due to expanded band tail states. However, despite the different TCOs, functional materials, architectures, and electricity output, outdoor-conditions simulations predict that all SSCs are expected to operate at similar temperatures with only ~1.5 °C maximum difference under real-world conditions, which is ~5 °C lower than in conventional silicon wafer-scaled solar cells. The resulting PCE difference for the ~1.5 °C temperature difference between the studied SSCs was found considerable, with (absolute) values around ~0.1–0.6%. Outdoor-conditions simulations also predict that the output-power losses for all examined SSCs are expected to be less than half of those in silicon solar cells.

We elucidate this behavior by showing that the impact of parasitic absorption (*e.g.*, in ETLs, HTLs, TCOs, and metals) on the temperature rise and output power losses becomes less important as λ_g increases, *e.g.*, as in tandem SSCs. However, we also show that tandem SSCs are bound to operate at higher device temperatures (and higher output-power losses relative to STC) than single-junction SSCs, despite their higher PCE and lower parasitic absorption, due to less efficient spectrum utilization, which is found to be a fundamental rather than an architectural constrain.

Consequently, following our analysis, we highlight pathways to depart from the effect of similar operating temperatures in thin-film SSCs by combining appropriate active layers and functional/transport materials. These improvements could reduce PCE losses by up to ~7 times compared to conventional silicon solar cells in real-world conditions (~5.8–11.2%$_{rel}$). Therefore, our analysis by including solar photons above λ_g expands current knowledge for more stable SSCs with higher PCEs and provides a new strategy and roadmap to aid the research challenge of optimal technology and material requirements.

Results and discussion

Fig. 1a–f (insets) shows the cross-sectional scanning electron microscopy (SEM) images of fabricated OSCs (Fig. 1a and b), PSCs (Fig. 1d and e), OSC/PSC (Fig. 1c), and PSC/PSC[7] (Fig. 1f); the SEM images are also shown in Fig. S2 (ESI†) at a larger scale for better clarity. They are realized in various architectures, *i.e.*, p–i–n (Fig. 1a and d), planar n–i–p (Fig. 1b), mesoscopic n–i–p (Fig. 1e), and tandems (Fig. 1c and f), composed of various HTLs (*i.e.*, PEDOT:PSS, 2PACz, MoO_x, NiO, and Spiro-OMeTAD), ETLs (*i.e.*, TiO_2, SnO_2, ZnO, PNDIT-F3N, C_{60}/BCP, and PDINN), TCOs (*i.e.*, ITO and FTO), and metal contacts (*i.e.*, Ag, Au, and Cu); see stacks' layout in Fig. S1a–f (ESI†). Moreover, highly-efficient active layers were selected, *i.e.*, PM6:L8-BO for OSCs ($\lambda_g \sim$ 900 nm),[1,2] $FAPbI_3$ for PSCs ($\lambda_g \sim$ 830 nm),[3–5] $Cs_{0.15}MA_{0.15}FA_{0.7}Pb(I_{0.6}Br_{0.4})_3$ and PM6:BTP-eC9:$PC_{71}BM$ for OSC/PSC ($\lambda_g \sim$ 910 nm),[6] and $Cs_{0.15}MA_{0.15}FA_{0.7}Pb(I_{0.6}Br_{0.4})_3$ and $FA_{0.7}MA_{0.3}Pb_{0.5}Sn_{0.5}I_3$ for PSC/PSC ($\lambda_g \sim$ 1020 nm).[7] Thus, present study incorporates the effect of material, λ_g, and architecture (*i.e.*, inverted, non-inverted, and tandems). We note that mesoscopic FTO-based n–i–p over planar ITO-based n–i–p PSC was examined given (i) the similar PCEs and λ_g of planar ITO-based n–i–p and p–i–n PSCs (Fig. 1d),[5,24] and (ii) FTO has recently emerged as a promising candidate to replace ITO for PSCs' commercialization due to its lower cost, sheet resistance (~8 Ω sq^{-1}), high thermal stability when treated, and performance.[4,17] Therefore, the study of FTO-based PSCs is also of great importance. Examined SSCs' solar absorptance spectra are

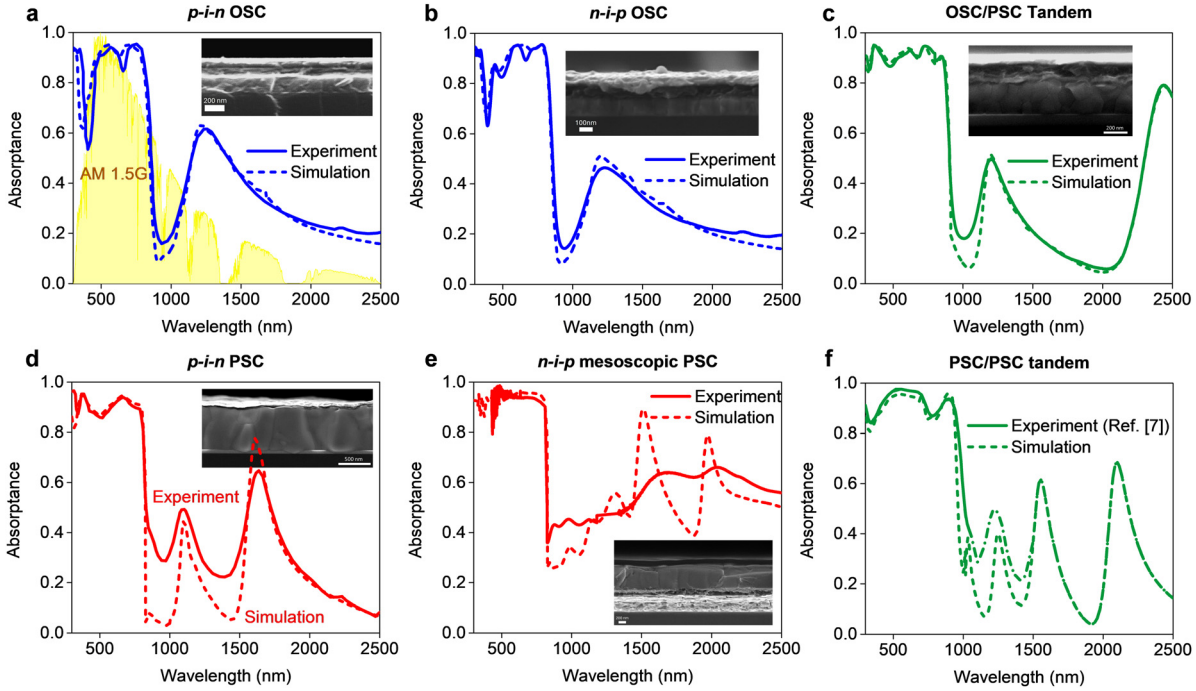

Fig. 1 Experimental (solid), simulated (dashed) absorptance spectra in 300–2500 nm, and scanning electron microscopy (SEM) cross-sectional images (insets) of examined SSCs: (a) p–i–n OSC (blue), (b) n–i–p OSC (blue), (c) OSC/PSC (green), (d) p–i–n PSC (red), (e) n–i–p mesoscopic PSC (blue), and (f) PSC/PSC (green), together with the AM 1.5G solar irradiance spectra (plotted only in (a) for clarity). Stacks' layout is shown in Fig. S1a–f (ESI†). The gray line in SEM images insets indicates the scale bar.

experimentally characterized in the 300–2500 nm wavelength range and are shown in Fig. 1a–f (solid).

In the range of ~300–λ_g nm, all SSCs show strong light absorption, as expected, since the photon energy is higher than active layers' band gap energy. Notably, all SSCs show substantial absorption also in the range λ_g–2500 nm, even though photons at these wavelengths have lower energy than active layers' band gap energy. Indicatively, from the measured absorptance spectra (Fig. 1a–f) and the AM1.5G (Fig. 1a), heat source in λ_g–2500 nm, *i.e.*, radiation intensity in λ_g–2500 nm converted into heat ($\int_{\lambda_g}^{2500\ \mathrm{nm}} I_{\mathrm{AM1.5G}}(\lambda)\alpha(\lambda)\mathrm{d}\lambda$, where $\alpha(\lambda)$ is the measured absorptance and $I_{\mathrm{AM1.5G}}(\lambda)$ is the solar illumination represented by the measured sun's radiation, the AM1.5G spectrum), is calculated to be 183, 138, 110, 92, 86, and 81 W m^{-2} in n–i–p mesoscopic PSC, p–i–n PSC, p–i–n OSC, n–i–p OSC, PSC/PSC, and OSC/PSC, respectively. This sub-band gap absorption ($\lambda > \lambda_g$) does not contribute to photocurrent and only heats SSCs due to parasitic absorption of IR photons at the various functional materials (*e.g.*, ETLs, HTLs, TCOs, or metal contacts), expected to substantially increase the device heat load and detrimentally affect device reliability/stability and PCE.

Given SSCs' thin film nature (~1 μm – see Experimental/theoretical methods) and technology versatility, the physical origin of the substantial parasitic heat source should be identified; specifically, what is the contribution of each layer/material and if sub-band gap absorption ($\lambda > \lambda_g$) is further enhanced by thin-film interference or light-trapping effects (*e.g.*, from surface roughness or textures). To answer these questions, we provide theoretical characterizations on SSCs' absorption properties in 300–2500 nm (Fig. 1a–f – dashed) and calculate parasitic absorption in each HTL, ETL, TCO, and metal contact (Fig. 2a–f) by employing the transfer matrix method assuming plane-parallel interfaces.[12,25]

First, a close agreement is observed in Fig. 1a–f between the simulated (dashed) and experimental absorptance spectra (solid). Slight discrepancies in ~850–1500 nm mainly for perovskite-based SSCs (Fig. 1d–f) are attributed to the extra sub-band gap absorption caused by the expanded band tail states in perovskites (see Fig. S11, ESI†).[26] We note that, given the comparable or even higher Urbach energies in organic compared to perovskite semiconductors[27,28] with a rather weak thickness dependence,[28] the more pronounced band tailing effect in PSCs (Fig. 1d and e) compared to OSCs (Fig. 1a–c) could be attributed to the higher optical path length in thicker perovskite films (~550–800 nm) than the other active layers (~90–250 nm). Notably, this agreement further confirms (in addition to the cross-sectional SEM images (insets)) that layer interfaces can be considered nearly planar in λ_g–2500 nm, which minimizes absorption due to light-trapping effects.

Moreover, this agreement (solid *versus* dashed curves in Fig. 1a–f) further enables and validates the evaluation of the absorption and heat generation in each layer/material. Specifically, as shown in Fig. 2a–f, parasitic heat source arises mainly from sub-band gap absorption ($\lambda > \lambda_g$) in TCOs, *i.e.*, ITO (Fig. 2a–d and f) and FTO (Fig. 2e). Consequently, the thermal response of SSCs is expected to be highly affected by the TCO properties, such as TCO material or thickness and sheet-resistance, due to the trade-off relationship between the transmittance (hence

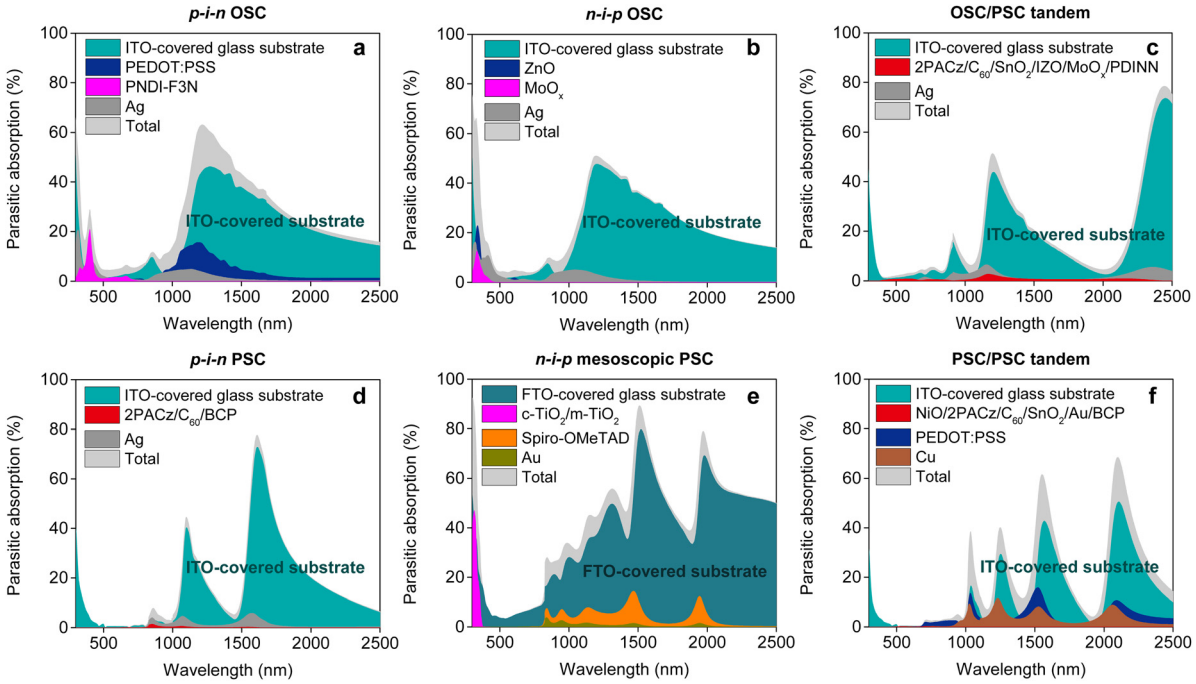

Fig. 2 Simulated parasitic absorption in each layer/material in 300–2500 nm of examined (a) p–i–n OSC, (b) n–i–p OSC, (c) OSC/PSC, (d) p–i–n PSC, (e) n–i–p mesoscopic PSC, and (f) PSC/PSC. Stacks' layout is shown in Fig. S1a–f (ESI†).

absorptance) and electrical conductance.[25] Indicatively, utilizing typical ~450-nm-thick TEC8 FTO (~8 Ω sq^{-1}) instead of ~120-nm-thick ITO (~10 Ω sq^{-1}) (Fig. 1d and e) leads to significantly higher parasitic absorption in λ_g–2500 nm (>45 W m^{-2}). Apart from TCOs (Fig. 2a–f), PEDOT:PSS (~30-nm-thick), Spiro-OMeTAD (~200-nm-thick), and Cu in λ_g–2500 nm (Fig. 2a, e and f) as well as TiO_2 (~30–200-nm-thick) and PNDIT-F3N (~5-nm-thick) in ultraviolet (UV) (~300–380 nm) (Fig. 2a and e) further increase the device parasitic absorption compared to other typical ETLs/HTLs and metal contacts, and, therefore, should be avoided for optimal thermal and optical management. Indicatively, the parasitic heat source in p–i–n OSC (~110 W m^{-2}) is higher than in n–i–p OSC (~92 W m^{-2}) mainly due to higher absorption in ~30-nm-thick PEDOT:PSS than ~40-nm-thick ZnO in λ_g–2500 nm (Fig. 2a and b). Moreover, it is observed that the increased heat source in p–i–n compared to n–i–p OSCs arises from the absorption properties of the ETL/HTL materials, rather than the architectural differences (inverted or non-inverted SSCs) that could influence PCE. Interestingly, Fig. 1d also shows that the expanded band tail states in perovskites (Fig. S11, ESI†) further increase PSCs' heat source significantly (~62.2 W m^{-2}), and is expected to seriously affect their thermal response and operating temperatures. Nevertheless, Fig. 1 and 2 indicate quite similar absorption in λ_g–2500 nm (except in the case of FTO). Specifically, all ITO-based SSCs absorb about ~20–33% of sub-band gap radiation ($\lambda > \lambda_g$) (Fig. 2a–d and f) compared to ~44% for FTO-based PSC (Fig. 2e). This result indicates that the amount of parasitic heat source in SSCs highly depends on λ_g. Specifically, due to similar parasitic absorption in λ_g–2500 nm (20–33%), a higher parasitic heat source is expected for SSCs with lower λ_g due to the higher solar irradiance at lower wavelengths (see Fig. 1a – yellow). Indicatively, the parasitic heat source in ITO-based p–i–n PSC (~138 W m^{-2}) of lower λ_g (~830 nm) is much higher than in ITO-based OSC/PSC (~81 W m^{-2}) and PSC/PSC (~86 W m^{-2}) of higher λ_g (~900–1000 nm).

Given SSCs' thin film nature (~1 μm), we also need to identify if sub-band gap absorption is further enhanced by thin-film interference effects (see absorption peaks in λ_g–2500 nm (Fig. 1a–f)). A theoretical analysis on two-pass absorption in ITO and FTO (Fig. S8, ESI†) reveals that absorption peaks in λ_g–2500 nm arise from thin-film interference mainly in the case of perovskite-based SSCs (Fig. 1c–f), which is attributed to the thicker perovskite (~550–800 nm) than organic active layers (~90–120 nm). Specifically, in the case of OSCs, the slightly asymmetric absorption peaks around ~1210 nm (Fig. 1a–c) mainly arise from increasing absorption with wavelength at $\lambda < 1210$ nm (increasing extinction coefficient; see Fig. S7a – green, ESI†) and increasing reflection with wavelength at $\lambda > 1210$ nm (impedance mismatch due to abrupt decrease of refractive index; see Fig. S7a – black, ESI†). Nevertheless, even in the case of more pronounced thin-film interference (Fig. 1c–f), the device heat source does not increase substantially (<25 W m^{-2}) compared to two-pass absorption (Fig. S8c–f, ESI†).

Fig. 1 and 2 revealed the physical origin of excess heat source in SSCs due to UV (~300–380 nm) and sub-band gap absorption (λ_g–2500 nm) and the important role of λ_g on SSCs' parasitic heat source. Next, to evaluate the impact of parasitic heat source on solar cell operation and efficiency, and definitely conclude on the impact of λ_g, *i.e.*, evaluate the relative impact of absorption also in ~300–λ_g nm, we examine, in

Fig. 3a–f, each spectral contribution on operating temperature and PCE of the examined SSCs for typical outdoor conditions (*i.e.*, ~1–4 m s^{-1} wind speed, 25 °C, 1000 W m^{-2} of solar radiation). Specifically, based on the experimental absorptance (Fig. 1a–f), we evaluate theoretically the impact of absorption in UV (~300–380 nm – blue), near and short-wave infrared (NIR-SWIR) (~λ_g–2500 nm – green), mid-infrared (MIR) (>4000 nm – red), and their combination UV-NIR-SWIR-MIR (black solid) relative to the absorption in visible (VIS) (~380–λ_g nm – black dashed) on PCE loss (ΔPCE(%$_{rel}$)) and on operating temperature (T) based on a combined thermal-optical-electrical analysis. Briefly, we first calculate the absorbed solar power in SSCs (*i.e.*, $\int_{300\ nm}^{2500\ nm} I_{AM1.5G}(\lambda)\alpha(\lambda)d\lambda$) based on measured absorptance (Fig. 1 – solid) and use it as a heat input in a coupled electro-thermal simulator. We then set up a coupled electro-thermal simulator that calculates T by solving the steady-state condition of solar cells' energy balance equation due to the energy exchange between solar cell and environment.[12,25] The temperature-dependent PCE is self-consistently determined by solving the steady-state problem by the linear relation PCE(T) = PCE$_{STC}$ × [1 + β_{PCE}/100 × (T − 25 °C)],[23] where PCE$_{STC}$ denotes SSCs' PCE at STC and β_{PCE} = dPCE/dT (%) the temperature coefficient of PCE normalized at % compared to the SSC operating at STC (see Fig. S3, ESI†). We refer to opto-electro-thermal modeling of SSCs in Experimental/theoretical methods for further details.

Interestingly, Fig. 3a–f shows that the operating temperature of all examined SSCs increases substantially by ~4.2–12.0 °C (black solid), despite their thin-film nature, mainly due to parasitic heat source in NIR-SWIR (~2.8–8.8 °C – green) as well as UV (~1.0–1.5 °C – blue) and sub-optimal radiative cooling in MIR (~1.2–2.4 °C – red), indicating sub-optimal thermal management in typical SSCs. Moreover, as expected (see Fig. S9c – black, ESI†), ΔT in NIR-SWIR (green) highly depends on λ_g, increasing as λ_g decreases. Indicatively, ΔT ~ 4.1–8.8 °C for

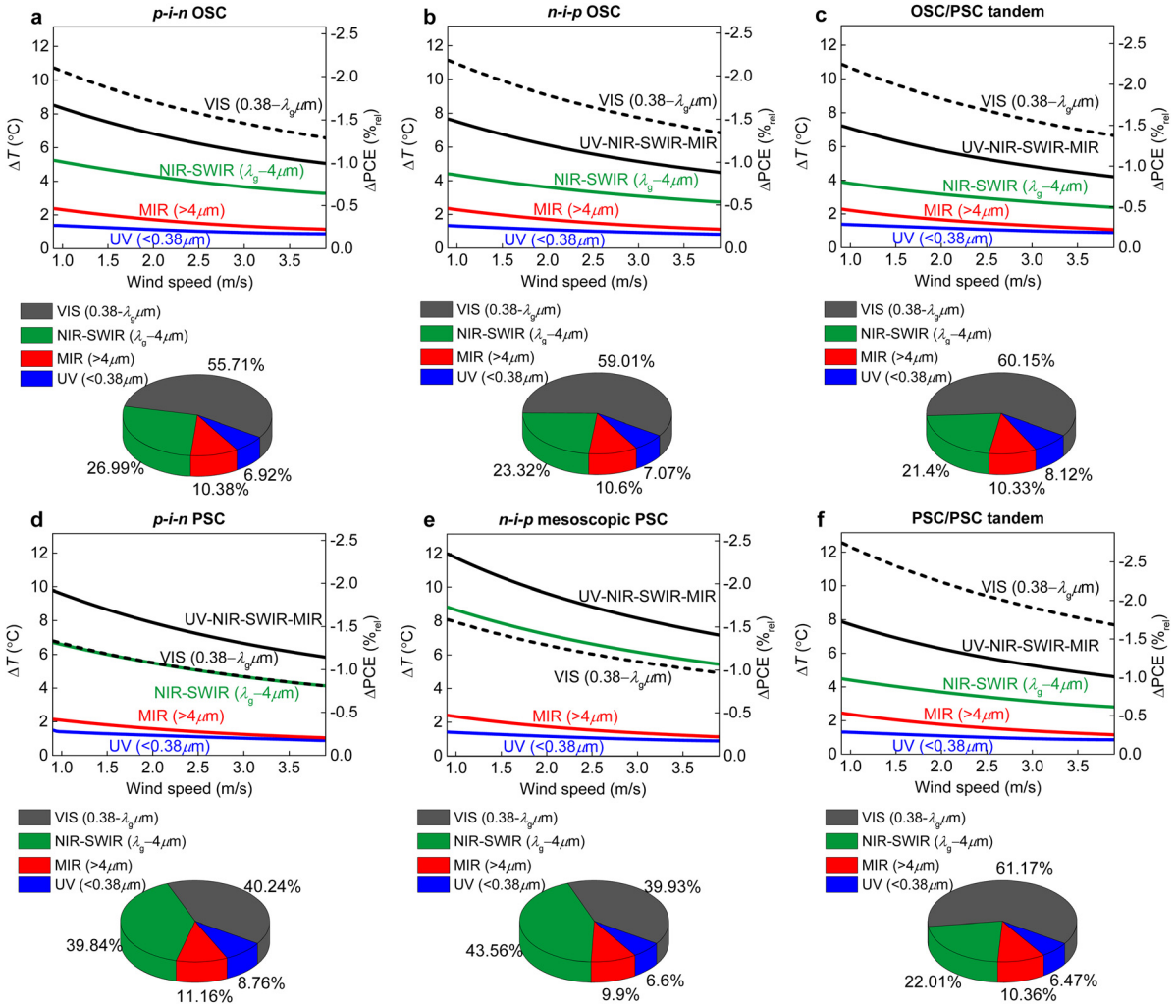

Fig. 3 Spectral contribution in SSCs' operating temperature rise (ΔT) and PCE loss (ΔPCE(%$_{rel}$)) from UV (> 300 nm) to MIR (< 30 000 nm) as a function of wind speed (~1–4 m s^{-1}) based on the experimental absorptance shown Fig. 1a–f. Top panels: Impact of absorption in UV (~300–380 nm – blue), VIS (~380–λ_g nm – black dashed), NIR-SWIR (λ_g–2500 nm – green), MIR (> 4000 nm – red), and combined UV-NIR-SWIR-MIR (black solid) on ΔT and ΔPCE(%$_{rel}$) for (a) p–i–n OSC (b) n–i–p OSC, (c) OSC/PSC, (d) p–i–n PSC, (e) n–i–p mesoscopic PSC, and (f) PSC/PSC. Bottom panels: Spectral contribution to ΔT and ΔPCE(%$_{rel}$) for each SSC [in %] assuming ~2.5 m s^{-1} wind speed.

p–i–n and n–i–p mesoscopic PSCs of lower λ_g (~830 nm) relative to ~2.4–5.2 °C for p–i–n, n–i–p OSCs, OSC/PSC, and PSC/PSC of higher λ_g (~900–1000 nm).

Operating temperature further increases by ~4.1–12.5 °C due to solar heating also in ~380–λ_g nm (VIS – black dashed). In contrast to ΔT in NIR-SWIR (green), ΔT in VIS (black dashed) increases mainly as λ_g increases (see also Fig. S9c – red, ESI†). Specifically, ΔT ~ 4.1–8.1 °C for p–i–n and n–i–p mesoscopic PSCs of lower λ_g (~830 nm) relative to ~6.6–12.5 °C for p–i–n, n–i–p OSCs, OSC/PSC, and PSC/PSC of higher λ_g (~900–1000 nm). A parametric analysis on T and PCE loss relative to STC (ΔPCE(%$_{rel,STC}$)) as a function of (i) λ_g, (ii) parasitic absorption, and (iii) PCE in STC (PCE$_{STC}$) (Fig. S4, ESI†) reveals that this effect arises from conversion losses due to the less efficient spectrum utilization as λ_g increases, which is found to be a fundamental rather than an architectural constrain, *i.e.*, not related to unoptimized PCE$_{STC}$ or parasitic absorption in ~300–λ_g nm. Indicatively, for PSC/PSC of much higher λ_g ($\lambda_g^{PSC/PSC}$ ~ 1020 nm *versus* λ_g^{PSC} ~ 830 nm), there is an obvious increase in ΔT and PCE loss in VIS (~0.38–λ_g nm) compared to p–i–n and n–i–p PSCs (see black dashed curves in Fig. 3f *versus* Fig. 3d and e). Specifically, due to this much higher λ_g, the extra absorbed solar power in PSC/PSC in the $\lambda_g^{PSC} - \lambda_g^{PSC/PSC}$ wavelength range is high and not overwhelmed by its ~10% higher electricity-output power (see Fig. S6b, ESI†). As a result, the PSC/PSC heat source generated in the active layer increases substantially compared to single-junction PSCs, hence T and PCE loss in ~0.38–λ_g nm (Fig. 3d–f).

Consequently, results in Fig. 1–3 indicate that SSCs of higher λ_g (including tandems despite their even higher PCE$_{STC}$) are bound to operate at higher device temperatures, hence higher output-power losses relative to STC. Moreover, as parasitic absorption increases in ~λ_g–2500 nm, the operating temperature of SSCs of lower λ_g is expected to increase at a higher rate than that of SSCs of higher λ_g (see Fig. S4a *versus* b, ESI†) due to due to higher photon energy at lower wavelengths (see also Fig. 1a – yellow). Therefore, all SSCs are expected to operate at similar temperatures in the absence of thermal management.

Extensive knowledge of SSCs' operation under real-world conditions is essential for their optimal application in the field. Therefore, we conducted outdoor-conditions simulations (see Experimental/theoretical methods) for actual environmental situations (see Fig. S5, ESI†), *i.e.*, time-dependent wind speed, solar irradiance, ambient temperature, and relative humidity.[22,23] The results are presented in Fig. 4 showing SSCs' time-dependent T (Fig. 4a and b) and ΔPCE(%$_{rel,STC}$) (Fig. 4c and d) during a day in August (Fig. 4a and c) and November (Fig. 4b and d).

Interestingly, Fig. 4a and b shows that all SSCs can reach high operating temperatures despite their thin-film nature, *i.e.*, >43 °C, >30 °C during a day in August and November, respectively. This is mainly due to conversion losses of fundamental nature in ~300–λ_g nm (Fig. 3a–f and Fig. S4a and b, ESI†) and substantial parasitic

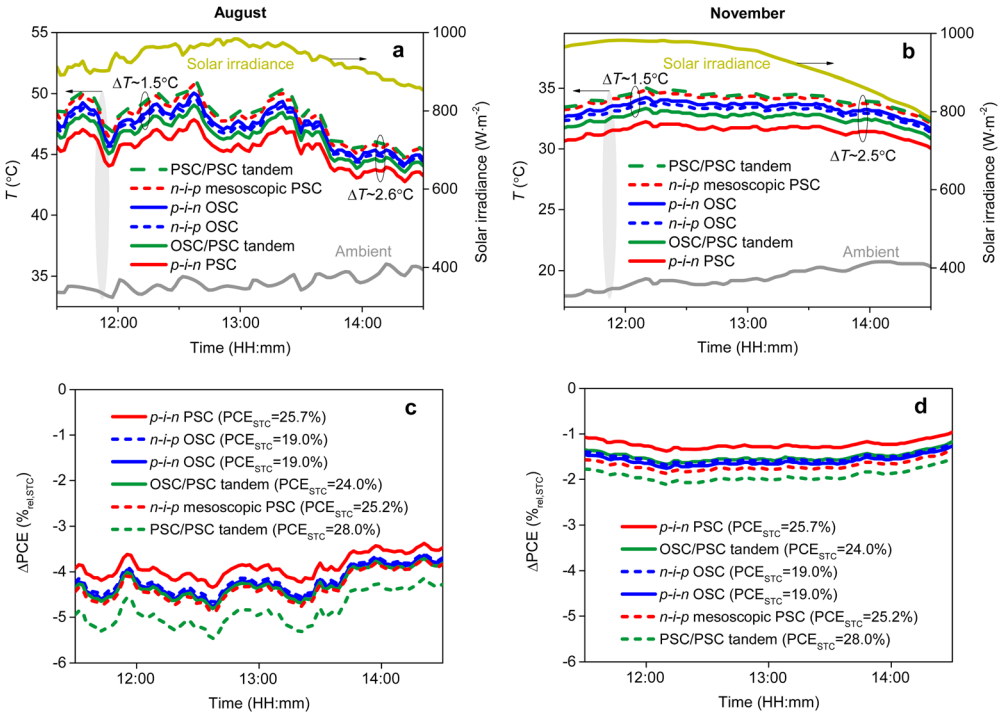

Fig. 4 Simulated time-dependent outdoor performance of the fabricated SSCs shown in Fig. 1a–f under real-world conditions during a day in August (a) and (c) and November (b) and (d). (a) and (b) Time-dependent device temperature (T) and (c) and (d) PCE losses relative to STC (ΔPCE(%$_{rel,STC}$)) for p–i–n OSC (blue solid), n–i–p OSC (blue dashed), OSC/PSC (green solid), p–i–n PSC (red solid), n–i–p mesoscopic PSC (red dashed), and PSC/PSC (green dashed). The time-dependent performance of SSCs is investigated by combining the experimental data of solar irradiance (yellow), ambient air temperature (gray), wind speed (Fig. S5c, ESI†), and relative humidity (Fig. S5d, ESI†).[22,23]

Table 1 Main sources of solar heating, ΔT relative to STC (25 °C), and ΔPCE($\%_{rel,STC}$) for each examined SSC

SSC	Main sources of solar heating	ΔPCE[$\%_{rel,STC}$]	ΔT [°C]
p–i–n OSC	High λ_g – related conversion losses	~1.3–4.8	~7–25
n–i–p OSC	High λ_g – related conversion losses	~1.2–4.7	~6–24
p–i–n PSC	Absorption in ITO/Exp. band tail states in perovskites/lower λ_g – related conversion losses	~1.0–4.3	~5–23
n–i–p mesosc. PSC	Absorption in FTO/Exp. band tail states in perovskites/lower λ_g – related conversion losses	~1.4–4.9	~7–26
OSC/PSC	High λ_g – related conversion losses	~1.2–4.8	~6–24
PSC/PSC	High λ_g – related conversion losses/Exp. band tail states in perovskites	~1.5–5.5	~7–26

absorption in TCOs in λ_g–2500 nm (Fig. 2a–f). We note that the main sources of solar heating for each examined SSC are summarized in Table 1. Specifically, all SSCs operate ~13 °C, ~14 °C higher than ambient temperature (gray) and ~22 °C, ~8 °C higher than STC (25 °C) in August and November, respectively. Their PCE also decreases due to their negative PCE-T coefficient ($\beta_{PCE} > -0.21\%_{rel}$ °C^{-1}, see Fig. S3, ESI†),[29,30] resulting in ΔPCE($\%_{rel,STC}$) ~ $-4.3\%_{rel}$ and $-1.6\%_{rel}$ in August and November, respectively (Fig. 4c and d). The corresponding ΔT relative to STC (25 °C) and ΔPCE($\%_{rel,STC}$) data are summarized in Table 1. Indicatively, at the same time, current industrial (silicon) passivated emitter and rear cells (PERC) operate at ~5 °C higher device temperature (Fig. S14a and b, ESI†) due to the much higher parasitic absorption in λ_g–2500 nm (Fig. S13a, ESI†). Notably, Fig. 4c, d and Fig. S14c, d (ESI†) also show that PCE losses for all examined SSCs are expected to be ~2–5 times lower than in conventional (silicon) PERC solar cells, due to PERC higher parasitic absorption (Fig. S13a, ESI†) and lower (or higher in absolute values) β_{PCE} ~ $-0.38\%_{rel}$ °C^{-1} (Fig. S3, ESI†). Specifically, for PERC solar cells ΔPCE($\%_{rel,STC}$) ~ $-11.2\%_{rel}$ and $-5.8\%_{rel}$ in August and November, respectively (Fig. S14c and d, ESI†), compared to -3.8–$4.9\%_{rel}$ and -1.2–$1.9\%_{rel}$ in SSCs, respectively (Fig. 4c and d).

Moreover, despite the different architectures, TCOs, functional/transport materials, and active layers, all SSCs operate at similar device temperatures with only ~1.5 °C maximum difference under real-world conditions (Fig. 4a and b), except in the case of p–i–n PSC (~2.6 °C). However, the resulting PCE difference for the ~1.5 °C temperature difference between the studied SSCs was found considerable, with (absolute) values around ~0.3–0.6% in August and ~0.1–0.3% in November. These results can be interpreted from SSCs' ΔPCE($\%_{rel,STC}$) and PCE_{STC} (see Fig. 4c and d). Interestingly, p–i–n PSC was able to depart from the effect of similar T in SSCs due to the lower λ_g (~830 nm) in conjunction with the absence of too high parasitic absorption in λ_g–2500 nm (see Fig. 2d *versus* Fig. 2e). Indicatively, SSCs of lower λ_g such as $FAPbI_3$- (λ_g ~ 830 nm),[4,5] $MAPbI_3$- (λ_g ~ 800 nm),[9] or CsFAPbIBr-based PSCs (λ_g ~ 700 nm)[7] can reach ΔPCE($\%_{rel,STC}$) as low as < $-1\%_{rel}$ no matter the weather conditions and independent of their β_{PCE} (see Fig. S4c, ESI†). In comparison, typical high-efficiency OSCs (*e.g.*, PM6:L8-BO- or PM6:BTP-eC9:PCBM-based)[1,2,6] are bound to operate at higher device temperatures (Fig. S4a and b, ESI†), hence PCE losses (Fig. S4c and d, ESI†), due to their higher λ_g (> ~900 nm) to achieve high photocurrent and PCE_{STC}. Accordingly, typical PSC/PSC tandems (*e.g.*, $FA_{0.7}MA_{0.3}Pb_{0.5}Sn_{0.5}I_3$-based) are also prone to higher T (see Fig. 4a and b or Fig. S4a and b, ESI†) and PCE losses relative to STC (see Fig. 4c and d or Fig. S4c and d, ESI†) due to higher λ_g (~1020 nm). We note that the higher ΔPCE($\%_{rel,STC}$) for PSC/PSC compared to SSCs in Fig. 4c and d is related both to its higher T (see Fig. 4a and b) and lower β_{PCE} (or higher in absolute values) (see red curve in Fig. S3, ESI†). Specifically, according to Shockley's and Queisser's limit, β_{PCE} decreases (or increases in absolute values) as λ_g increases (see black curve in Fig. S3, ESI†) and further decreases (with the number of sub-cells) in tandem configurations.[31,32] These results also imply that thermal management is more critical in SSCs of lower λ_g like in PSCs. Indicatively, a p–i–n PSC could operate at even lower T in the absence of band tail states in perovskites (see Fig. S12a and b, ESI†), and, therefore, even lower ΔPCE($\%_{rel,STC}$) ~ $-0.9\%_{rel}$ (Fig. S12d, ESI†), that is ~7 times lower than in silicon solar cells (Fig. S14d, ESI†).

To understand the physical behavior of SSCs under real-world conditions, in Fig. 5, we address heat generation, dissipation, and energy conversion processes when operating outdoors. Specifically, we theoretically calculate [in W m^{-2}] the time-dependent device heat load (Fig. 5a) (see eqn (6)) arising from the interplay of parasitic absorption in ~300–2500 nm (Fig. 5d) and conversion losses in ~300–λ_g nm (Fig. 5e), the electricity output (Fig. 5f) (see eqn (6)), and the radiative (Fig. 5b) (see eqn (2)–(4)), non-radiative heat dissipation (Fig. 5c) (see eqn (5)) due to infrared emission and convection-conduction (*e.g.*, winds), respectively.

First, Fig. 5a and f shows that most of the absorbed solar radiation by SSCs converts into heat (Fig. 5a) rather than electrical power (Fig. 5f), increasing operating temperature above ambient (Fig. 4a). Specifically, 73.1%, 72.7%, 64.0%, 68.1%, 67.2%, and 66.2% of absorbed solar radiation converts to 462.2, 453.2, 439.6, 410.7, 480.1, and 487.2 W m^{-2} of solar heating during noontime in August (Fig. 5a) in p–i–n OSC, n–i–p OSC, OSC/PSC, p–i–n PSC, n–i–p mesoscopic PSC, and PSC/PSC, respectively. As shown in Fig. 5d and e, solar heating (Fig. 5a) arises mainly from conversion losses (Fig. 5e and Table 1) of fundamental nature (Fig. S4, ESI†) as well as substantial parasitic absorption (Fig. 5d) mainly in TCOs in ~λ_g–2500 nm (Fig. 2a–f and Table 1).

Interestingly, the highest heat load is generated in PSC/PSC (Fig. 5a – green dashed) despite the highest electricity output (Fig. 5f – green dashed) and lowest parasitic absorption than all examined single-junction SSCs (Fig. 5d), due to higher λ_g (~1020 nm), hence higher conversion losses (Fig. 5e – green dashed). The physical origin of higher conversion losses in PSC/PSC is the higher heat source generated in the active layer mainly between their band edges, *i.e.*, $\lambda_g^{PSC} - \lambda_g^{PSC/PSC}$ (see Fig. S6b, ESI†). More specifically, the extra absorbed solar power in PSC/PSC in the $\lambda_g^{PSC} - \lambda_g^{PSC/PSC}$ wavelength range

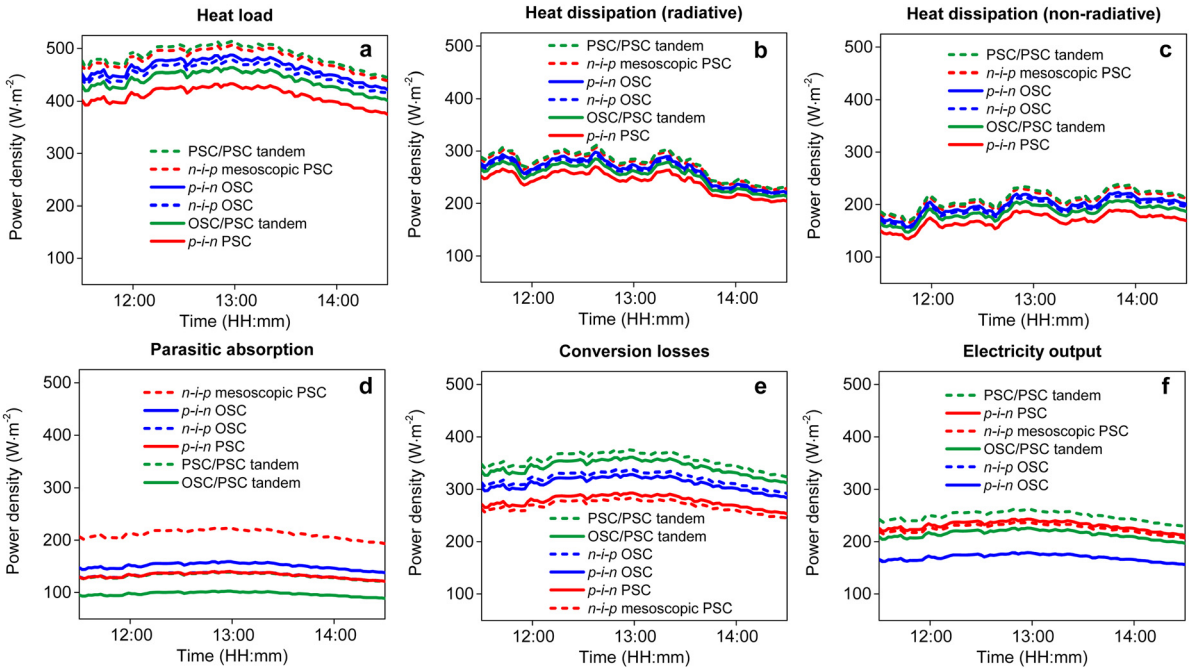

Fig. 5 Simulated time-dependent (a) heat load, (b) radiative and (c) non-radiative heat dissipation, (d) parasitic absorption, (e) conversion losses, and (f) electricity output of fabricated p–i–n OSC (blue solid), n–i–p OSC (blue dashed), OSC/PSC (green solid), p–i–n PSC (red solid), n–i–p mesoscopic PSC (red dashed), and PSC/PSC (green dashed) operating under real-world conditions during a day in August. The time-dependent performance of SSCs is investigated by combining the experimental data of solar irradiance (Fig. S5a, ESI†), ambient air temperature (Fig. S5b, ESI†), wind speed (Fig. S5c, ESI†), and relative humidity (Fig. S5d, ESI†).[22,23]

due to its higher λ_g ($\lambda_g^{PSC/PSC} > \lambda_g^{PSC}$) is not overwhelmed by its higher electricity-output power (see Fig. S6b, ESI†). Therefore, tandem SSCs are expected to operate at higher device temperatures than optimal single-junction SSCs (see also Fig. S4a and b, ESI†), hence higher output-power losses relative to STC. Indicatively, PSC/PSC loses about 10–15% of its PCE_{STC} advantage compared to a p–i–n PSC when operating in real-world conditions (green dashed *versus* red solid curves in Fig. 5f) due to inherently inferior thermal response. This considerable thermal effect should also be considered alongside the impact of current mismatch in real-world conditions,[33] to fully assess the benefits of tandem SSCs. We note that the magnitude of heat and electricity output difference between SSCs may be affected by incident source, *e.g.*, actual solar (see green and black (AM1.5G) curves in Fig. S6a, ESI†) or solar simulators' spectral irradiance used in the lab (see red curves in Fig. S6a, ESI†).

Fig. 5b and c also highlights the importance of SSCs' radiative properties (reflection/absorption/emission) beyond λ_g also in MIR (>4 μm), especially for outdoor operation at elevated temperatures, *e.g.*, in summer. Specifically, average heat dissipation through emission of infrared electromagnetic radiation (>4 μm) equals ~261.3, ~213.8 W m^{-2} (see eqn (2)–(4)) during noontime in August (Fig. 5b) and November (Fig. S15b, ESI†), respectively, compared to ~194.3, ~233.1 W m^{-2} (see eqn (5)) through convection-conduction (*e.g.*, winds) (Fig. 5c and Fig. S15c, ESI†). This is because releasing heat through thermal emission scales approximately with $\sim T^3 - T^4$ (see Fig. S10d, ESI†) while convection mainly depends on winds (see Fig. 5c and Fig. S5c – green, ESI†). Interestingly, our calculations indicate up to ~44 W m^{-2} further available cooling load by enhancing SSCs' absorptivity/emissivity in the atmospheric transparency window (~8–13 μm) (see eqn (2)–(4) and Fig. S10d, ESI†).[22,23,34,35]

Conclusion

In summary, we provide full spectral characterization beyond the band gap wavelengths (~300–2500 nm) and optical-thermal-electrical analysis on the most prominent tandem and single-junction SSCs. The objective was to access the influence of IR light beyond λ_g on SSCs operation, in order to uncover the physical origin and interplay of parasitic absorption (~300–2500 nm) and conversion losses (~300–λ_g nm). As a result, our analysis, by incorporating solar photons above λ_g, expands current knowledge for more stable SSCs with higher PCEs and unveils optimal architectures, material requirements, and conditions for optimal operation of SSCs with lower device temperatures and PCE losses even up to ~7 times lower compared to conventional (silicon) wafer-scaled solar cells.

Taking into consideration that lately SSCs have become market products,[36] it is also interesting to relate the outcomes of this work with currently established SSC technology for commercialization. For instance, right now, most SSCs incorporate ITO as the front contact. However, results in Fig. 2, 3 and Fig. S8, S9 (ESI†) identify ITO as the main cause of parasitic heat source in SSCs, indicating sub-optimal thermal management. Recently, FTO emerged as a promising candidate to replace ITO in PSCs.[4,17] However, results in Fig. 1–3 indicate

that FTO not only increases solar heating substantially compared to ITO but it is even less appropriate for PSCs (where it is mostly used) due to typical perovskites' lower λ_g, boosting parasitic heat source (see Fig. 5d – red dashed). Consequently, exploring novel transparent conductive electrodes (TCEs) and materials with minimal absorption in NIR-SWIR such as low-absorbing single-layer graphene, carbon nanotubes, metal-mesh, or ultrathin TCO–metal–TCO (or insulator–metal–insulator),[37–39] is also essential for optimal thermal management, especially as λ_g decreases (like in PSCs). Given TCO advantages, a thin multilayer filter on top of the glass substrate or integrated on the TCO could reflect unwanted solar radiation, leading to >6 °C temperature reduction (see also Fig. 3e).[40] We note that, according to our calculations, ~ 20 W m^{-2} of heat source reduction in SSCs leads roughly to ~ 1 °C operating temperature decrease for typical environmental conditions (Fig. S5, ESI†) and SSCs (Fig. 1 and Fig. S10, ESI†), *e.g.*, see blue curves in Fig. 4a and b.

Regarding SSC technology or architecture, interestingly, the present analysis also shows that despite the common belief, typical tandem SSCs utilize less efficiently the solar spectrum than optimal single-junction SSCs despite mitigating thermodynamic losses such as thermalization. These results highlight an additional mechanism of substantial PCE loss in tandem SSCs, besides current mismatch upon field application. To this end, typical OSCs of relatively high λ_g ($> \sim 900$ nm) as in tandem SSCs and much lower PCE_{STC} ($< \sim 19\%$) are also prone to higher operating temperatures and PCE losses relative to STC. Therefore, pathways to increase their PCE_{STC} more effectively, *e.g.*, with increasing voltage compared to increasing photocurrent *via* increasing λ_g, seem more promising for optimal thermal management in OSCs. Finally, present analysis also shows that thermal management is more critical to PSCs (especially FTO-based) due to their lower λ_g. Moreover, the expanded band tail states in perovskites have also been identified as a major cause of elevated operating temperatures in PSCs (see Fig. 1d and Fig. S11, S12, ESI†). Consequently, utilizing single-crystal[41] or thinner perovskites[42] than optimum ~ 800 nm in conjunction with more sophisticated TCEs could overcome or significantly mitigate PCE losses of SSCs relative to STC.

To sum up, given the wide range of the organic and perovskite semiconductors with continuously tunable band gaps and technology versatility (numerous HTLs, ETLs, TCOs, or metal contacts), by incorporating solar photons above λ_g, we identify and evaluate the materials, conditions, and λ_g requirements for optimal design and use of SSCs.

Methods

p–i–n and n–i–p OSCs preparation

Patterned indium tin oxide (ITO)-coated glass substrates purchased from Huananxianhcheng Ltd (China) (25 mm × 25 mm with a sheet resistance < 15 Ω sq^{-1}) were first cleaned by sonicating in a 2% v/v Hellmanex in deionized water solution for 20 min. The substrates were then rinsed with deionized water and sonicated for a further 15 min. Thereafter, they were sequentially cleaned in acetone and 2-propanol in an ultrasonic bath at ≈ 30 °C for 15 min each and blow-dried with nitrogen. Before coating the substrates were subjected to an UV-ozone process (Jetlight Company In. MODEL 24) for 15 min before fabrication.

p–i–n OSC. A ~ 30-nm-thick PEDOT:PSS thin film was deposited on top of the precleaned ITO-coated substrates by spin-coating and baked at 150 °C for 15 min. The solution of PM6 : L8-BO (1 : 1.2 w/w, 16.5 mg mL^{-1} in total) in chloroform with 1,4-diiodobenzene as a solid additive (the content of 1,4-diiodobenzene is 50% of the total mass of donor and acceptor) were advance and then spin-coated on top of the PEDOT:PSS layer. The prepared films were treated with thermal annealing at 85 °C for 5 min. After cooling to room temperature, a ~ 5-nm-thick PNDIT-F3N (0.5 mg mL^{-1} in methanol with 0.5% acetic acid, v/v) was spin-coated on the top of the active layer. Then, the samples were transferred into the evaporating chamber (Angstrom EvoVac) system inside the glove box and a 100-nm-thick silver (Ag) layer was thermally evaporated on the PNDIT-F3N layer.

n–i–p OSC. A ~ 40-nm-thick ZnO film (Avantama N-10-flex solution) was deposited on top of the precleaned ITO-coated substrates by spin-coating and baked at 120 °C for 20 min. The solution of PM6 : L8-BO (1 : 1.2 w/w, 16.5 mg mL^{-1} in total) in chloroform with 1,4-diiodobenzene as a solid additive (the content of 1,4-diiodobenzene is 50% of the total mass of donor and acceptor) were advance and then spin-coated on top of the ZnO layer. The prepared films were thermally annealed at 85 °C for 5 min. After cooling to room temperature, the samples were transferred to an evaporator (moorfield) placed outside the glove box and the precursor of molybdenum(VI) oxide was thermally evaporated at low rates to obtain a ~ 8-nm-thick MoO_x thin film on the top of the active layer. Then, the samples were transferred into the evaporating chamber (Angstrom EvoVac) system inside the glove box and a 100-nm-thick silver (Ag) layer was thermally evaporated on the MoO_x layer.

p–i–n and n–i–p OSCs characterization

Ultraviolet-visible (UV-Vis) absorption, transmittance spectra. The transmittance and reflectance spectra were performed by Varian Cary 5000 UV-Vis-NIR spectrophotometer. In reflectance mode the measurements were obtained by fitting the spectral and diffuse reflectance accessory (integrated sphere).

Scanning electron microscope images. The surface morphologies were studied by SEM (Jeol JSM7100F) with a spatial resolution of 1.2 nm at 30 kV. The microscope is fitted with a thermo scientific triple analysis system, featuring an UltraDry EDS detector, a MagnaRay parallel beam WDS spectrometer and a Lumis system for electron backscatter diffraction (EBSD).

p–i–n PSC and OSC/PSC preparation

Glass/ITO substrates (10 Ω sq^{-1}) were purchased from Xinyan Technology Ltd. Formamidinium iodide (FAI, 99.99% purity) and methylammonium bromide (MABr, 99.99% purity) and were acquired from GreatCell Solar Ltd. Lead(II) bromide (PbBr2, 99.999% purity), lead iodide(II) (PbI_2, 99.999% purity)

and cesium iodide (CsI, 99.999% purity), were purchased from Alfa Aesar. Molybdenum(VI) oxide (MoO_3, 99.97%) was purchased from Sigma-Aldrich. Poly[(2,6-(4,8-bis(5-(2-ethylhexyl-3-fluoro)thiophen-2-yl)-benzo[1,2-*b*:4,5-*b*′]dithiophene))-*alt*-(5,5-(1′,3′-di-2-thienyl-5′,7′-bis(2-ethylhexyl)benzo[1′,2′-*c*:4′,5′-*c*′]dithiophene-4,8-dione)] (PM6), 2,2′-[[12,13-bis(2-butyloctyl)-12,13-dihydro-3,9-dinonylbisthieno[2″,3″:4′,5′]thieno[2′,3′:4,5]pyrrolo[3,2-*e*:2′,3′-*g*][2,1,3]benzothiadiazole-2,10-diyl]bis[methylidyne(5,6-chloro-3-oxo-1*H*-indene-2,1(3*H*)-diylidene)]]-bis[propanedinitrile] (BTP-eC9), [6,6]-phenyl-C71-butyric acid methyl ester (PC71BM) and *N*,*N*′-bis{3-[3-(dimethylamino)propylamino]propyl}perylene-3,4,9,10-tetracarboxylic diimide (PDINN) were from Solarmer Materials Inc. (2-(9*H*-Carbazol-9-yl)ethyl)phosphonic acid (2PACz) was purchased from TCI Chemicals. All materials were used as received without any purification process.

p–i–n PSC. Glass/ITO substrates were cleaned in a three-step procedure including sonication in detergent, acetone, and isopropanol for 15 minutes each. The substrates were dried with nitrogen flow prior to UV-ozone treatment for 20 minutes. Next, a 2PACz solution (0.3 mg mL^{-1} in absolute ethanol) was spin-coated at 3000 rpm for 30 seconds and thermally annealed at 100 °C for 10 minutes. The perovskite precursor solution was prepared by dissolving FAI, CsI, and PbI_2 in a mixture of DMF : DMSO (4 : 1) solvent obtaining a 1.6 M composition of $Cs_{0.05}FA_{0.85}PbI_3$. The precursor solution was spin-coated on the 2PACz-coated substrates at 4000 rpm for 50 seconds. Ethyl acetate was dropped 20 seconds before the end of the spin-coating process as an antisolvent. The samples were then annealed at 100 °C for 30 minutes. Finally, 30 nm of C_{60}, 7 nm of BCP, and 100 nm of Ag were thermally evaporated to complete the devices.

OSC/PSC. Perovskite-organic tandem solar cells were fabricated following a previously reported procedure.[6] Briefly, the wide-bandgap perovskite was prepared by dissolving CsI, FAI, MABr, $PbBr_2$, and PbI_2 in a mixture of DMF : DMSO (4 : 1) solvent to achieve a composition of $Cs_{0.15}MA_{0.15}FA_{0.70}Pb(I_{0.6}Br_{0.4})_3$ and a thickness of approximately 260 nm. After depositing 20 nm of C_{60}, a recombination layer consisting of SnO_2 (20 nm) and IZO (2 nm) was deposited using atomic layer deposition (ALD) and (radio frequency) RF sputtering, respectively. Next, 10 nm of MoO_x was thermally evaporated followed by a spin-coating of a 2PACz solution. The narrow-bandgap bulk heterojunction (BHJ) was prepared by dissolving PM6, BTP-eC9 and $PC_{71}BM$ with a ratio of 1 : 1.2 : 0.2 in anhydrous chloroform obtaining a thickness of approximately 100 nm. Finally, 5 nm of PDINN and 100 nm of Ag were deposited to complete the tandem devices.

p–i–n PSC and OSC/PSC characterization

Transmittance and reflectance properties of single-junction and tandem devices were measured using a Cary 5000 UV-Vis-NIR Spectrophotometer with light illumination was from the glass side. Top-view and cross-section scanning electron microscope (SEM) images were acquired using a Helios 5 UX (Thermo Scientific) microscope at an accelerating voltage of 5 kV.

n–i–p mesoscopic PSC preparation

Fluorine-doped tin oxide (FTO) glass substrates (TCO glass, TEC8) were etched using Zn powder and diluted hydrochloric acid (HCl), cleaned by ultrasonication in Hellmanex (2%, deionized water), deionized water, acetone, and ethanol. After drying the substrates with a nitrogen gun, they were UV-O_3 treated for 15 min. Afterwards, an approximately 20-nm-thick blocking layer (TiO_2) was deposited on the FTO by spray pyrolysis at 450 °C using a commercial titanium diisopropoxide bis(acetylacetonate) solution (75% in 2-propanol, Sigma-Aldrich) diluted in anhydrous ethanol (1 : 9 volume ratio) as a precursor and oxygen as a carrier gas. A mesoporous TiO_2 layer was deposited by spin-coating a diluted paste (Dyesol 30NRD) in ethanol (1 : 6 weight ratio) at 4000 rpm for 15 s and sintering at 450 °C for 30 min in a dry-air atmosphere. The perovskite films were deposited from the precursor solution, which was prepared in an argon atmosphere by dissolving FAI, MABr, PbI_2 and $PbBr_2$ in anhydrous dimethylformamide/dimethyl sulfoxide (4 : 1 volume ratio) to achieve the desired compositions $(FAPbI_3)_{0.98}(MAPbBr_3)_{0.02}$ using a 3% PbI_2 excess and 44 mg of MACl. The perovskite precursor was deposited in a dry-air atmosphere on FTO/c-TiO_2/m-TiO_2 substrate, using a single-step deposition method (6000 rpm for 50 seconds). To control the film crystallization, 10 seconds before the end of the spin-coating program, the perovskite precursor was quenched with chlorobenzene as the antisolvent. To form and crystallize the perovskite, the spin-coated perovskite precursors were annealed at 150 °C for 30 minutes inside a dry-air atmosphere. Subsequently, the perovskite films were then passivated by spin-coating (6000 rpm for 50 s) a 3 mg mL^{-1} dispersion of octylamonium iodide (OAI) in isopropanol. The ~200-nm-thick HTL (Spiro-OMeTAD doped with bis(trifluoromethylsulfonyl)imide lithium salt (17.8 μL of a solution of 520 mg of LiTFSI in 1 mL of acetonitrile) and 28.8 μL of 4-*tert*-butylpyridine)) was deposited by spin-coating at 4000 rpm for 30 s. Finally, an approximately 80 nm gold (Au) layer was deposited by thermal evaporation.

n–i–p mesoscopic PSC characterization

Fourier-transform infrared spectroscopy (FT-IR) measurements were carried out under vacuum, with a Bruker Vertex 70v FT-IR vacuum spectrometer (Bruker Optik GmbH, Rosenheim, Germany); the transmission of the samples was evaluated using a PIKE universal sample holder (PIKE Technologies, Inc. – Madison, USA), while reflection was measured using a Bruker Optics A513 reflection accessory (Bruker Optik GmbH, Rosenheim, Germany), at an angle of incidence of 7-degrees. To cover a spectral range of 0.45–25 μm, two different sets of optics were used: (a) for 0.45–1.25 μm, a quartz beamsplitter and a room temperature silicon diode detector, while (b) for 1.3–25 μm), a broad band KBr beamsplitter and a room temperature broad band triglycine sulfate (DTGS) detector were used. In any case, interferograms were collected at 4 cm^{-1} resolution (8 scans), apodized with a Blackman–Harris function, and Fourier transformed with two levels of zero filling to yield spectra encoded at 2 cm^{-1} intervals. Before scanning the samples, an empty holder and an aluminum mirror (>90% average reflectivity) background measurement was recorded in vacuum for transmission and reflection measurements, respectively, and each sample spectrum was obtained by automatic subtraction of it.

Opto-electro-thermal modeling of SSCs

We perform a combined thermal-optical-electrical analysis to calculate power conversion efficiency (PCE) as a function of the operating temperature (T) of the encapsulated SSCs (see Fig. S10a–c, ESI†). First, we calculate the absorbed solar power in the encapsulated SSCs based on SSCs' measured absorptance (Fig. 1 – solid) and use it as the heat input in the electro-thermal simulation. We then set up a coupled electro-thermal simulator solving the steady-state energy balance for solar cells, with which we simulate T and the PCE as a function of solar irradiance, ambient temperature, relative humidity, and wind speed to mimic typical outdoor conditions:[12,25]

$$P_r(T) + P_c(T, T_a) + P_g(T, T_a) = P_h(T) + P_a(T_a), \quad (1)$$

In eqn (1), $P_h(T)$ is the heat flux from solar radiation and $P_a(T_a)$ is the radiative heat flux from the atmosphere, absorbed by the device at ambient temperature, T_a (*i.e.*, the right-hand side of eqn (1) includes/concerns the input heat-flux channels). $P_r(T)$ is the total heat flux radiated by SSCs at T, $P_c(T, T_a)$ accounts for the outgoing nonradiative heat transfer, and $P_g(T, T_a)$ is the radiative heat flux by the rear surface of SSCs. These power terms are given by[12,25]

$$P_r(T) = \int_0^\infty \int_0^{2\pi} \int_0^{\pi/2} I_{BB}(\lambda, T)\varepsilon(\lambda, \theta, \varphi)\cos\theta \sin\theta d\theta d\varphi d\lambda, \quad (2)$$

$$P_a(T_a) = \int_0^\infty \int_0^{2\pi} \int_0^{\pi/2} I_{BB}(\lambda, T_a)\varepsilon(\lambda, \theta, \varphi)\varepsilon_a(\lambda, \theta)\cos\theta \sin\theta d\theta d\varphi d\lambda, \quad (3)$$

$$P_g(T, T_a) = \sigma\varepsilon_r A(T^4 - T_a^4), \quad (4)$$

$$P_c(T_c, T_a) = h_c(T_c - T_a), \quad (5)$$

$$P_h(T) = \int_0^\infty I_{AM1.5G}(\lambda)\varepsilon(\lambda)d\lambda - \mathrm{PCE}\,(T)\int_0^\infty I_{AM1.5G}(\lambda)d\lambda, \quad (6)$$

where λ is the free-space wavelength, σ is the Stefan–Boltzmann constant, $A \sim 1$ is the view factor, $I_{BB}(\lambda, T)$ is the spectral intensity of a blackbody at temperature T given by Planck's law, $I_{AM1.5G}(\lambda)$ is the solar illumination represented by the measured sun's radiation, the AM1.5G spectrum, and $h_{c,top}$ and $h_{c,bottom}$ are the wind-speed-dependent nonradiative heat transfer coefficients (higher h_c values correspond to stronger winds) at the top and rear surfaces of the solar cell, respectively. For $h_{c,top}$ and $h_{c,bottom}$, we use two relations, frequently used in previous studies for similarly encapsulated solar cell systems, expressed as $h_{c,top} = 5.8 + 3.7v_w$ and $h_{c,bottom} = 2.8 + 3.0v_w$, where v_w is the velocity of wind at the module surface [in m s^{-1}] given by the relationship suggested in the literature $v_w = 0.68v_f - 0.5$, where v_f is the wind speed measured by the closest weather station.[43] $\varepsilon(\lambda, \theta, \varphi)$ is SSCs' spectral directional emissivity (equal to spectral directional absorptivity, according to Kirchhoff's law) (see Fig. S10a–c – black, ESI†), $\varepsilon_a(\lambda,\theta) = 1 - t(\lambda)^{1/\cos\theta}$ is the angle-dependent emissivity of the atmosphere, with $t(\lambda)$ the atmospheric transmittance in the zenith direction affected by humidity, ambient temperature, and clouds (see Fig. S5d, ESI†), and $\varepsilon_r \sim 0.9$ is the solar cell rear surface hemispherical emissivity (see Fig. S10a–c – red, ESI†). Due to energy conservation, P_h equals the difference between absorbed solar energy flux and generated electrical power in the solar cell, where PCE(T) is the temperature-dependent cell's solar-to-electrical power conversion efficiency assuming that it operates at its maximum power point (mp); it is given by the linear relation $\mathrm{PCE}(T) = \mathrm{PCE}_{STC} \times [1 + \beta_{PCE}/100 \times (T - 25\ ^\circ\mathrm{C})]$,[23] where PCE_{STC}(298.15 K) is SSCs' output power at standard test conditions (STC, *i.e.*, 1000 W m^{-2} of solar radiation, T = 25 °C) (see captions in Fig. 4c and d) and β_{PCE} = dPCE/dT (%) is the temperature coefficient of PCE normalized at % compared to the SSC operating at STC (see Fig. S3, ESI†). In eqn (6), we assume that the structure is facing the sun at a fixed angle. Thus, the term P_h does not have an angular integral, and SSCs' absorptance is represented by its value at normal incidence (see Fig. 1 – solid).

Author contributions

G. P. and G. K. conceived the idea of this project. G. P., G. K., A. P. and T. M. discussed and planned the experiments and simulations. G. P. performed the simulations and analysis related to them. A. P. fabricated and characterized the organic solar cells. T. M. and C. A. fabricated and characterized the perovskite and tandem solar cells. G. P. and G. K. wrote the first draft. A. P., T. M., C. A., E. A. A., S. F., M. H., A. C. T., G. Kenanakis., K. P., T. D. A. S. R. P. S., M. G. and M. K. revised the first draft and contributed towards finalizing the manuscript. G. K. supervised the project. All authors contributed to the preparation of the final manuscript and approved its submission for publication.

Data availability

The data supporting this article have been included as part of the ESI.†

Conflicts of interest

There are no conflicts to declare.

Acknowledgements

This work was supported by the Hellenic Foundation for Research and Innovation (HFRI) under "Sub-action 2 for Funding Projects in Leading-Edge Sectors – RRFQ: Basic Research Financing (Horizontal support for all Sciences)", Project ID 15117 (MultiCool).

References

1 L. Zhu, M. Zhang, J. Xu, C. Li, J. Yan, G. Zhou, W. Zhong, T. Hao, J. Song, X. Xue, Z. Zhou, R. Zeng, H. Zhu, C. C. Chen, R. C. I. MacKenzie, Y. Zou, J. Nelson, Y. Zhang, Y. Sun and F. Liu, *Nat. Mater.*, 2022, **21**(6), 656–663.

2 J. Huang, J. Fu, B. Yuan, H. Xia, T. Chen, Y. Lang, H. Liu, Z. Ren, Q. Liang, K. Liu, Z. Guan, G. Zou, H. T. Chandran, T. W. B. Lo, X. Lu, C. S. Lee, H. L. Yip, Y. K. Peng and G. Li, *Nat. Commun.*, 2024, **15**(1), 1–14.
3 J. Jeong, M. Kim, J. Seo, H. Lu, P. Ahlawat, A. Mishra, Y. Yang, M. A. Hope, F. T. Eickemeyer, M. Kim, Y. J. Yoon, I. W. Choi, B. P. Darwich, S. J. Choi, Y. Jo, J. H. Lee, B. Walker, S. M. Zakeeruddin, L. Emsley, U. Rothlisberger, A. Hagfeldt, D. S. Kim, M. Grätzel and J. Y. Kim, *Nature*, 2021, **592**(7854), 381–385.
4 M. Kim, J. Jeong, H. Lu, T. K. Lee, F. T. Eickemeyer, Y. Liu, I. W. Choi, S. J. Choi, Y. Jo, H. B. Kim, S. I. Mo, Y. K. Kim, H. Lee, N. G. An, S. Cho, W. R. Tress, S. M. Zakeeruddin, A. Hagfeldt, J. Y. Kim, M. Grätzel and D. S. Kim, *Science*, 2022, **375**, 302–306.
5 S. Zhang, F. Ye, X. Wang, R. Chen, H. Zhang, L. Zhan, X. Jiang, Y. Li, X. Ji, S. Liu, M. Yu, F. Yu, Y. Zhang, R. Wu, Z. Liu, Z. Ning, D. Neher, L. Han, Y. Lin, H. Tian, W. Chen, M. Stolterfoht, L. Zhang, W. H. Zhu and Y. Wu, *Science*, 2023, **380**, 404–409.
6 T. Maksudov, M. He, S. Doukas, M. I. Nugraha, B. Adilbekova, H. Faber, L. Luo, R. Zhou, O. M. Bakr, W. Ogieglo, I. Pinnau, G. T. Harrison, D. R. Naphade, Z. Ling, E. Lidorikis, S. Fatayer, M. Heeney, F. H. Isikgor and T. D. Anthopoulos, *Mater. Sci. Eng., R*, 2024, **159**, 100802.
7 R. Lin, Y. Wang, Q. Lu, B. Tang, J. Li, H. Gao, Y. Gao, H. Li, C. Ding, J. Wen, P. Wu, C. Liu, S. Zhao, K. Xiao, Z. Liu, C. Ma, Y. Deng, L. Li, F. Fan and H. Tan, *Nature*, 2023, **620**(7976), 994–1000.
8 S. Liu, L. Hao, J. Yu, Y. Xu, Y. Dou, J. Xie, Y. Wang, K. Zhang, F. Huang and Y. Cao, *ACS Nano*, 2024, **19**, 759.
9 Z. Chen, B. Turedi, A. Y. Alsalloum, C. Yang, X. Zheng, I. Gereige, A. Alsaggaf, O. F. Mohammed and O. M. Bakr, *ACS Energy Lett.*, 2019, **4**, 1258–1259.
10 Z. Sun, H. Ma, T. L. H. Mai, J. Park, S. Jeong and C. Yang, *ACS Nano*, 2024, **19**, 43.
11 X. Zhang, X. Wu, J. Zhang, X. Kong, J. Li, A. Li, Z. Li, X. Li, M. Zhang, G. Yang, Y. Li and C. Sun, *ACS Nano*, 2024, **19**, 900–910.
12 G. Perrakis, A. C. Tasolamprou, G. Kenanakis, E. N. Economou, S. Tzortzakis and M. Kafesaki, *ACS Photonics*, 2022, **9**, 1327–1337.
13 T. Ma, Y. An, Z. Yang, Z. Ai, Y. Zhang, C. Wang and X. Li, *Adv. Funct. Mater.*, 2023, **33**, 2212596.
14 Z. Ai, T. Ma, Y. Zhang, Y. Bao, L. Shi, Z. Yang, Y. Zhan, L. Qin, G. Cao and X. Li, *Small*, 2024, **20**, 2404012.
15 W. Li, S. Buddhiraju and S. Fan, *Light: Sci. Appl.*, 2020, **9**, 2047–7538.
16 Z. Liu, R. Lin, M. Wei, M. Yin, P. Wu, M. Li, L. Li, Y. Wang, G. Chen, V. Carnevali, L. Agosta, V. Slama, N. Lempesis, Z. Wang, M. Wang, Y. Deng, H. Luo, H. Gao, U. Rothlisberger, S. M. Zakeeruddin, X. Luo, Y. Liu, M. Grätzel and H. Tan, *Nat. Mater.*, 2025, **2025**, 1–8.
17 S. M. Park, M. Wei, N. Lempesis, W. Yu, T. Hossain, L. Agosta, V. Carnevali, H. R. Atapattu, P. Serles, F. T. Eickemeyer, H. Shin, M. Vafaie, D. Choi, K. Darabi, E. D. Jung, Y. Yang, D. Bin Kim, S. M. Zakeeruddin, B. Chen, A. Amassian, T. Filleter, M. G. Kanatzidis, K. R. Graham, L. Xiao, U. Rothlisberger, M. Grätzel and E. H. Sargent, *Nature*, 2023, **624**(7991), 289–294.
18 O. Dupré, R. Vaillon and M. A. Green, *Sol. Energy Mater. Sol. Cells*, 2015, **140**, 92–100.
19 B. Dong, M. Wei, Y. Li, Y. Yang, W. Ma, Y. Zhang, Y. Ran, M. Cui, Z. Su, Q. Fan, Z. Bi, T. Edvinsson, Z. Ding, H. Ju, S. You, S. M. Zakeeruddin, X. Li, A. Hagfeldt, M. Grätzel and Y. Liu, *Nat. Energy*, 2024, **2025**, 1–12.
20 Y. Lin, Y. Zhang, A. Magomedov, E. Gkogkosi, J. Zhang, X. Zheng, A. El-Labban, S. Barlow, V. Getautis, E. Wang, L. Tsetseris, S. R. Marder, I. McCulloch and T. D. Anthopoulos, *Mater. Horiz.*, 2023, **10**, 1292–1300.
21 Y. W. Noh, J. M. Ha, J. G. Son, J. Han, H. Lee, D. W. Kim, M. H. Jee, W. G. Shin, S. Cho, J. Y. Kim, M. H. Song and H. Y. Woo, *Mater. Horiz.*, 2024, **11**, 2926–2936.
22 L. Zhu, A. P. Raman and S. Fan, *Proc. Natl. Acad. Sci. U. S. A.*, 2015, **112**, 12282–12287.
23 Z. Li, S. Ahmed and T. Ma, *Sol. RRL*, 2021, **5**, 2000735.
24 X. Zhao, Y. Qiu, M. Wang, D. Wu, X. Yue, H. Yan, B. Fan, S. Du, Y. Yang, Y. Yang, D. Li, P. Cui, H. Huang, Y. Li, N. G. Park and M. Li, *ACS Energy Lett.*, 2024, **9**, 2659–2669.
25 G. Perrakis, A. C. Tasolamprou, G. Kakavelakis, K. Petridis, M. Graetzel, G. Kenanakis, S. Tzortzakis and M. Kafesaki, *Sci. Rep.*, 2024, **14**(1), 1–14.
26 Z. Wei, J. He, Y. Shi, Q. Li, Q. Niu, Y. Hou and S. Yang, *Sol. Energy*, 2023, **264**, 112040.
27 C. Zhang, S. Mahadevan, J. Yuan, J. K. W. Ho, Y. Gao, W. Liu, H. Zhong, H. Yan, Y. Zou, S. W. Tsang and S. K. So, *ACS Energy Lett.*, 2022, **7**, 1971–1979.
28 C. Kaiser, O. J. Sandberg, N. Zarrabi, W. Li, P. Meredith and A. Armin, *Nat. Commun.*, 2021, **12**(1), 1–9.
29 S. Pescetelli, A. Agresti, G. Viskadouros, G. Viskadouros, S. Razza, K. Rogdakis, I. Kalogerakis, E. Spiliarotis, E. Leonardi, P. Mariani, L. Sorbello, M. Pierro, C. Cornaro, S. Bellani, L. Najafi, B. Martín-García, A. Esaú, D. R. Castillo, R. Oropesa-Nuñez, M. Prato, S. Maranghi, M. L. Parisi, A. Sinicropi, R. Basosi, F. Bonaccorso, E. Kymakis and A. Di Carlo, *Nat. Energy*, 2022, **2022**, 1–11.
30 G. Bardizza, E. Salis, C. Toledo and E. D. Dunlop, *Prog. Photovoltaics Res. Appl.*, 2020, **28**, 593–600.
31 S. Y. Heo, D. H. Kim, Y. M. Song and G. J. Lee, *Adv. Energy Mater.*, 2022, **12**, 2103258.
32 P. Testa, M. Cagnoni and F. Cappelluti, *Sol. Energy Mater. Sol. Cells*, 2024, **274**, 112958.
33 M. T. Hörantner, T. Leijtens, M. E. Ziffer, G. E. Eperon, M. G. Christoforo, M. D. McGehee and H. J. Snaith, *ACS Energy Lett.*, 2017, **2**, 2506–2513.
34 F. Xie, W. Jin, J. R. Nolen, H. Pan, N. Yi, Y. An, Z. Zhang, X. Kong, F. Zhu, K. Jiang, S. Tian, T. Liu, X. Sun, L. Li, D. Li, Y.-F. Xiao, A. Alu, S. Fan and W. Li, *Science*, 2024, **386**, 788–794.
35 G. Perrakis, A. C. Tasolamprou, G. Kenanakis, E. N. Economou, S. Tzortzakis and M. Kafesaki, *Sci. Rep.*, 2021, **11**(1), 1–10.

36 Oxford PV starts commercial distribution of perovskite solar modules – pv magazine International, https://www.pv-magazine.com/2024/09/05/oxford-pv-starts-commercial-distribution-of-perovskite-solar-modules/, (accessed 19 January 2025).
37 R. A. Maniyara, V. K. Mkhitaryan, T. L. Chen, D. S. Ghosh and V. Pruneri, *Nat. Commun.*, 2016, 7(1), 1–8.
38 A. Panagiotopoulos, T. Maksudov, G. Kakavelakis, G. Perrakis, E. A. Alharbi, D. Kutsarov, F. H. Isikgor, S. Alfihed, K. Petridis, M. Kafesaki, S. R. P. Silva, T. D. Anthopoulos and M. Graetzel, *Appl. Phys. Rev.*, 2023, **10**, 41303.
39 A. Ghaffari, Z. Saki, N. Taghavinia, M. M. Byranvand and M. Saliba, *Mater. Horiz.*, 2022, **9**, 2473–2495.
40 W. Li, Y. Shi, K. Chen, L. Zhu and S. Fan, *ACS Photonics*, 2017, **4**, 774–782.
41 T. Zhao, R. He, T. Liu, Y. Li, D. Yu, Y. Gao, G. Qu, N. Li, C. Wang, H. Huang, J. Zhou, S. Bai, S. Xiao, Z. Chen, Y. Chen and Q. Song, *ACS Nano*, 2025, **19**(3), 3282–3292.
42 G. Perrakis, G. Kakavelakis, A. C. Tasolamprou, E. A. Alharbi, K. Petridis, G. Kenanakis and M. Kafesaki, *ACS Appl. Energy Mater.*, 2024, **7**, 8963.
43 L. Xu, W. Liu, H. Liu, C. Ke, M. Wang, C. Zhang, E. Aydin, M. Al-Aswad, K. Kotsovos, I. Gereige, A. Al-Saggaf, A. Jamal, X. Yang, P. Wang, F. Laquai, T. G. Allen and S. De Wolf, *Joule*, 2021, **5**, 631–645.

